Microwave Image Reconstruction of Tissue Property Dispersion Characteristics Utilizing Multiple Frequency Information

Qianqian Fang, *Student Member, IEEE,* Paul M. Meaney, *Member, IEEE,* and Keith D. Paulsen, *Member, IEEE*

***Abstract*— A multiple frequency dispersion reconstruction (MFDR) algorithm utilizing a Gauss-Newton iterative strategy is presented for microwave imaging. This algorithm facilitates the simultaneous use of multiple frequency measurement data in a single image reconstruction. Using the stabilizing effects of the low frequency measurement data, higher frequency data can be included to reconstruct images with improved resolution. The parameters reconstructed in this implementation are now frequency independent dispersion coefficients instead of the actual properties and may provide new diagnostic information. In this paper, large high-contrast objects are successfully constructed utilizing assumed simple dispersion models for both simulation and phantom cases for which the traditional single frequency algorithm previously failed. Consistent improvement in image quality can be observed by involving more frequencies in the reconstruction; however, there appears to be a limit to how closely spaced the frequencies can be chosen while still providing independent new information. Possibilities for fine-tuning the image reconstruction performance in this context include 1) variations of the assumed dispersion model, and 2) Jacobian matrix column and row weighting schemes. Techniques for further reducing the forward solution computation time using time-domain solvers are also briefly discussed. The proposed dispersion reconstruction technique is quite general and can also be utilized in conjunction with other Gauss-Newton based algorithms including log-magnitude phase-form (LMPF) algorithm.**

***Index Terms*— microwave imaging, multiple frequency dispersion reconstruction, column weighting, row weighting, FDTD**

I. Introduction

Microwave imaging has been investigated for potential medical applications for several decades [1]. Several published studies on tissue electrical properties have demonstrated significant contrast between different organs and tissue types over a wide frequency range [2], [3]. The dominant physiological factor distinguishing these properties is water content [4] which can vary from roughly 15% or less for adipose tissue and bone to almost 100% for blood, muscle and many internal organs [5]. Consequently, several investigators have shown that the properties of certain pathological conditions such as ischemic heart wall [6], [7], breast tumors [3], [8], and leukemia [9] exhibit considerable electrical property contrast with their corresponding normal tissue. These contrast mechanisms have been the motivating factors driving investigators to exploit microwave imaging in a diagnostic capacity [10], [12]–[14]. Other features such as strong correlation of the tissue properties with temperature may also be exploited in temperature monitoring schemes required in thermal therapies such as hyperthermia [15], [16].

Historically, microwave imaging approaches have taken many forms. Tomographic approaches utilizing filtered back projection [17]–[19] with various schemes such as the Born and Rytov approximations being used in the early 1980's with limited success [20]. While these approaches were well suited for ultrasound computed tomography where the contrast in tissue speeds of sound varied within a narrow range (excluding bone and air) [21], [22], Slaney *et al* [23] demonstrated that these linear approaches degraded rapidly for higher contrast cases making them impractical for microwave imaging of anatomical sites. Similar tomographic approaches such as the chirp radar technique [24] have been investigated for temperature monitoring applications also in low contrast environments.

Investigations have also been conducted into the use of passive radiometry for medical applications. Jacobsen and Stauffer [25] have developed a multi-frequency radiometer integrated with a therapy device which allows them to spatially monitor tissue temperature to several centimeters below the skin surface. This phenomenon exploits the fact that molecules radiate broadband black-body electromagnetic signals in proportion to their temperature [26]. While infrared systems are used to detect surface temperatures, the microwave spectrum is ideally suited for detecting signals at considerable depth corresponding to subsurface temperature variations. This phenomenon has been used in monitoring temperatures during thermal therapy with a multiple frequency approach [25], [27] and monitoring the internal brain temperatures of newborn infants [28]. This approach is currently being applied to the problem of breast cancer detection where presumably the tumor temperature is greater than that of the surrounding tissue due to its higher metabolism rate [29]–[31].

Confocal imaging approaches utilizing primarily backscattered signal data are currently being investigated by Hagness *et al* [11], [12] and Fear *et al* [13], [14] for breast cancer detection. They utilize approaches similar to synthetic aperture techniques currently used in ultrasound backscatter imaging [32], [33] to synthetically focus the beam from all antennas in an array sequentially to all points within the 3-D imaging

Manuscript received October 20 2003; revised February 3 2004. This work was supported in part by National Institutes of Health (NIH) through the National Cancer Institute under Grant P01-CA80139.

The authors are with Thayer School of Engineering, Dartmouth College, Hanover, NH 03755 USA (e-mail: qianqian.fang@dartmouth.edu, paul.m.meaney@dartmouth.edu, keith.d.paulsen@dartmouth.edu)

domain. The strongest return signals are associated with zones having the highest contrast (i.e. the tumor) with respect to the normal tissue. This microwave effect has been primarily simulation-based to date with some initial phantom experiments [14], [34] to explore the feasibility of developing a patient interface for this approach. Finally, researchers have also been investigating thermoacoustic approaches which utilize the high contrast of the electrical properties in combination with the higher spatial resolution of acoustic imaging [35], [36]. In these approaches, the breast is illuminated with a short, high-power microwave pulse which induces mechanical vibration of the tissue (i.e. heating). The microwave signals preferentially deposit more energy in the malignant tissue than the normal breast tissue because of the significantly higher permittivity and conductivity. The associated vibrations are subsequently detected by ultrasound receivers and displayed as images. Preliminary phantom results are quite promising.

Over the past decade, with the advent of dramatically improved computational capabilities, several researchers have explored the use of non-linear inverse scattering approaches in tomographic modes. Several groups, including Caorsi *et al* [37], Joachimowicz *et al* [38] and Liu *et al* [39] have demonstrated in simulations the ability to recover 2-D and 3-D property distributions utilizing a range of regularization protocols. Meaney *et al* [10], [40] have developed a 2-D clinical system for breast cancer detection along with a thermal imaging system for *in vivo* animal experiments [16]. In both of these cases, an iterative Gauss-Newton approach is used to reconstruct an image of the tissue property distribution [41], [42]. Semenov *et al* [6], [7] has also developed inverse scattering strategies and utilized them with their whole body imaging device in attempts to detect *in vivo* infarction of canine cardiac tissue. All of these approaches are generally ill-posed and require some level of regularization to stabilize the convergence to a viable solution [42]–[44].

Typically, the iterative inverse scattering approaches collect data at receiver sites about the imaging zone associated with multiple electromagnetic illuminations. The solutions generally improve with increased amounts of measured data [45]. These reconstruction algorithms have usually only been applied utilizing single operating frequencies with the lower frequency reconstructed images appearing smoother and with less detail but also exhibiting more stable convergence behavior to a viable solution compared with the less stable higher frequency cases. However, increasing the amount of data through reconstructions utilizing data from multiple frequency (MF) illuminations could prove to be a powerful way to improve the image quality.

Unlike the frequency-hopping approach of Chew and Lin [46] and multi-frequency work of Haddadin *et al* [47], in which the spectral data were applied sequentially, we have developed a multi-frequency approach where the spectral data contribute to a single image reconstruction simultaneously. The following sections discuss the implementation of this approach along with possible characteristic relationships for the permittivity and conductivity frequency dispersions. A parameter scaling approach is also discussed since scaling of the recovered dispersion coefficients is a considerably different problem than just scaling the electrical properties for a single frequency problem [48]. The results section illustrates the strength of this algorithm in three challenging cases: two simulations and an analogous phantom experiment. The large high-contrast object imaging cases were chosen because the standard, single frequency algorithm converged to non-useful images for the higher frequency cases and produced only very smoothed imaged for the lower frequency reconstructions. Only by using the combination of data from both the lower and higher frequencies was the algorithm able to recover well-resolved images of the targets.

II. Theory

A. MF Dispersion Reconstruction Algorithm

Assuming time dependence of $\exp(j\omega t)$, the complex wave number squared, k^2, for non-magnetic isotropic media can be written as

$$\begin{aligned} k^2 &= \omega^2\mu_0\varepsilon(\omega) \\ &= \omega^2\mu_0\left\{\varepsilon_r(\omega)\varepsilon_0 - j\frac{\sigma(\omega)}{\omega}\right\} \\ &= k_R^2 - jk_I^2 \end{aligned} \tag{1}$$

where ω is angular frequency, $k_R^2 = \omega^2\mu_0\varepsilon_0\varepsilon_r(\omega)$ and $k_I^2 = \omega\mu_0\sigma(\omega)$ are the real and imaginary constituents of k^2, $\varepsilon_r(\omega)$ and $\sigma(\omega)$ are the relative permittivity and conductivity with associated frequency dependence, respectively, and ε_0 and μ_0 are the permittivity and magnetic permeability of free space, respectively.

Multiple dispersion models exist with varying degrees of complexity and appropriateness [49]–[52]. Without loss of generality, we can express the dispersion relationships in terms of non-dispersive coefficients as

$$\begin{aligned} \varepsilon_r(\omega) &= \varepsilon_r\left(\omega, \lambda_1, \lambda_2, \cdots, \lambda_M\right) \\ \sigma(\omega) &= \sigma\left(\omega, \gamma_1, \gamma_2, \cdots, \gamma_N\right) \end{aligned} \tag{2}$$

where $\lambda_i \quad (i = 1, 2, \cdots, M)$ and $\gamma_i \quad (i = 1, 2, \cdots, N)$ are the frequency independent dispersion coefficients for the M and N term relationships, $\varepsilon_r(\omega)$ and $\sigma(\omega)$, respectively.

The first order Gauss-Newton method assumes (from a truncated Taylor series with respect to k_R^2 and k_I^2) [41]

$$\begin{aligned} \Delta E_R &= \frac{\partial E_R}{\partial k_R^2}\Delta k_R^2 + \frac{\partial E_R}{\partial k_I^2}\Delta k_I^2 \\ \Delta E_I &= \frac{\partial E_I}{\partial k_R^2}\Delta k_R^2 + \frac{\partial E_I}{\partial k_I^2}\Delta k_I^2 \end{aligned} \tag{3}$$

where vectors ΔE_R and ΔE_I are the real and imaginary part of the difference between measured and calculated fields, respectively. The lengths of vectors ΔE_R and ΔE_I are equal to the total measurement data $TR = T \times R$, where T denotes the number of transmitters and R denotes the number of receivers per transmitter. Vectors k_R^2 and k_I^2 are length P, which is the number of unknown property parameters. The derivative terms in (3) are all matrices of size $TR \times P$. Combining equations (1), (2) and (3), applying the chain rule and assuming single frequency operation initially yields

$$\begin{aligned} \Delta E_R &= \sum_{i=1}^{M}\frac{\partial E_R}{\partial k_R^2}\frac{\partial k_R^2}{\partial \lambda_i}\Delta\lambda_i + \sum_{i=1}^{N}\frac{\partial E_R}{\partial k_I^2}\frac{\partial k_I^2}{\partial \gamma_i}\Delta\gamma_i \\ \Delta E_I &= \sum_{i=1}^{M}\frac{\partial E_I}{\partial k_R^2}\frac{\partial k_R^2}{\partial \lambda_i}\Delta\lambda_i + \sum_{i=1}^{N}\frac{\partial E_I}{\partial k_I^2}\frac{\partial k_I^2}{\partial \gamma_i}\Delta\gamma_i \end{aligned} \tag{4}$$

which can subsequently be written in matrix form

$$\begin{bmatrix} \mathbf{J}_R^R & \mathbf{J}_I^R \\ \mathbf{J}_R^I & \mathbf{J}_I^I \end{bmatrix} \begin{Bmatrix} \Delta\mathbf{l} \\ \Delta\mathbf{g} \end{Bmatrix} = \begin{Bmatrix} \Delta E_R \\ \Delta E_I \end{Bmatrix} \tag{5}$$

The components of the Jacobian matrix $[\mathbf{J}]$ are

$$\begin{aligned} \mathbf{J}_R^R &= \left[\frac{\partial E_R}{\partial k_R^2}\frac{\partial k_R^2}{\partial \lambda_1} \middle| \frac{\partial E_R}{\partial k_R^2}\frac{\partial k_R^2}{\partial \lambda_2} \middle| \cdots \middle| \frac{\partial E_R}{\partial k_R^2}\frac{\partial k_R^2}{\partial \lambda_M} \right] \\ \mathbf{J}_I^R &= \left[\frac{\partial E_R}{\partial k_I^2}\frac{\partial k_I^2}{\partial \gamma_1} \middle| \frac{\partial E_R}{\partial k_I^2}\frac{\partial k_I^2}{\partial \gamma_2} \middle| \cdots \middle| \frac{\partial E_R}{\partial k_I^2}\frac{\partial k_I^2}{\partial \gamma_N} \right] \end{aligned}$$

with $\mathbf{J}_R^I$ and $\mathbf{J}_I^I$ having corresponding definitions. $\mathbf{J}_R^R$ and $\mathbf{J}_R^I$ are submatrices with dimensions $(TR) \times (P \times M)$ whereas $\mathbf{J}_I^R$ and $\mathbf{J}_I^I$ are $(TR) \times (P \times N)$. $\Delta\mathbf{l} = \{\Delta\lambda_1, \Delta\lambda_2, \cdots, \Delta\lambda_M\}^T$, and $\Delta\mathbf{g} = \{\Delta\gamma_1, \Delta\gamma_2, \cdots, \Delta\gamma_N\}^T$ are the frequency independent property updates solved for at each iteration. By solving equation (5) at each iteration, the dispersion coefficient lists, i.e. $\{\lambda_1, \lambda_2, \cdots, \lambda_M\}$ and $\{\gamma_1, \gamma_2, \cdots, \gamma_N\}$, can be updated by

$$\begin{aligned} \{\lambda_1, \lambda_2, \cdots, \lambda_M\}_{s+1} &= \{\lambda_1, \lambda_2, \cdots, \lambda_M\}_s + \Delta\mathbf{l}_s^T \\ \{\gamma_1, \gamma_2, \cdots, \gamma_N\}_{s+1} &= \{\gamma_1, \gamma_2, \cdots, \gamma_N\}_s + \Delta\mathbf{g}_s^T \end{aligned} \tag{6}$$

where s is the iteration index. Essentially, the images are comprised of the dispersion coefficient distributions. As before, the dielectric profiles at any specified frequency in the investigating band can be readily calculated from equation (2). Additionally, the reconstructed dispersion coefficients themselves might provide new diagnostic information by capturing the dispersion signature of the tissues over a range of frequencies. For a given dispersion relationship, the terms $\frac{\partial k^2}{\partial \lambda_i}$ and $\frac{\partial k^2}{\partial \gamma_i}$ in (4) can be computed analytically. The details for deriving $\frac{\partial E}{\partial k^2}$ can be found in Fang *et al*. [53].

Since $\Delta\mathbf{l}$ and $\Delta\mathbf{g}$ are frequency independent, equation (5) can be generalized to F frequencies by expanding the Jacobian matrix on the left and electric field difference vector on the right

$$\begin{bmatrix} \mathbf{J}_R^R(\omega_1) & \mathbf{J}_I^R(\omega_1) \\ \mathbf{J}_R^I(\omega_1) & \mathbf{J}_I^I(\omega_1) \\ \mathbf{J}_R^R(\omega_2) & \mathbf{J}_I^R(\omega_2) \\ \mathbf{J}_R^I(\omega_2) & \mathbf{J}_I^I(\omega_2) \\ \cdots & \cdots \\ \mathbf{J}_R^R(\omega_F) & \mathbf{J}_I^R(\omega_F) \\ \mathbf{J}_R^I(\omega_F) & \mathbf{J}_I^I(\omega_F) \end{bmatrix} \begin{Bmatrix} \Delta\mathbf{l} \\ \Delta\mathbf{g} \end{Bmatrix} = \begin{Bmatrix} \Delta E_R(\omega_1) \\ \Delta E_I(\omega_1) \\ \Delta E_R(\omega_2) \\ \Delta E_I(\omega_2) \\ \cdots \\ \Delta E_R(\omega_F) \\ \Delta E_I(\omega_F) \end{Bmatrix} \tag{7}$$

Note that the Jacobian matrix and ΔE terms are now functions of frequency. Equation (7) is the generic form for MFDR and is valid for both 2-D and 3-D cases since the dispersion characteristics for an isotropic medium are dimensionless. It is also valid for vector or scalar forward models with dispersive or non-dispersive medium. Additionally, the MFDR technique can be combined, without loss of generality, with the log-magnitude/phase form (LMPF) approach which has demonstrated improved performance in certain circumstances such as with the recovery of large high-contrast objects [40]. The MFDR expression for the LMPF algorithm is

$$\begin{bmatrix} \mathbf{J}_R^\Gamma(\omega_1) & \mathbf{J}_I^\Gamma(\omega_1) \\ \mathbf{J}_R^\Phi(\omega_1) & \mathbf{J}_I^\Phi(\omega_1) \\ \mathbf{J}_R^\Gamma(\omega_2) & \mathbf{J}_I^\Gamma(\omega_2) \\ \mathbf{J}_R^\Phi(\omega_2) & \mathbf{J}_I^\Phi(\omega_2) \\ \cdots & \cdots \\ \mathbf{J}_R^\Gamma(\omega_F) & \mathbf{J}_I^\Gamma(\omega_F) \\ \mathbf{J}_R^\Phi(\omega_F) & \mathbf{J}_I^\Phi(\omega_F) \end{bmatrix} \begin{Bmatrix} \Delta\mathbf{l} \\ \Delta\mathbf{g} \end{Bmatrix} = \begin{Bmatrix} \Delta\Gamma(E(\omega_1)) \\ \Delta\Phi(E(\omega_1)) \\ \Delta\Gamma(E(\omega_2)) \\ \Delta\Phi(E(\omega_2)) \\ \cdots \\ \Delta\Gamma(E(\omega_F)) \\ \Delta\Phi(E(\omega_F)) \end{Bmatrix} \tag{8}$$

where Γ and Φ symbolize the log-magnitude and unwrapped phase of the electric fields, respectively. In this situation, the modified Jacobian terms can be expressed as

$$\begin{aligned} \mathbf{J}_R^\Gamma &= \frac{E_R\mathbf{J}_R^R + E_I\mathbf{J}_R^I}{E_R^2 + E_I^2} \\ \mathbf{J}_I^\Gamma &= \frac{E_R\mathbf{J}_I^R + E_I\mathbf{J}_I^I}{E_R^2 + E_I^2} \\ \mathbf{J}_R^\Phi &= \frac{E_R\mathbf{J}_R^R - E_I\mathbf{J}_R^R}{E_R^2 + E_I^2} \\ \mathbf{J}_I^\Phi &= \frac{E_R\mathbf{J}_I^R - E_I\mathbf{J}_I^R}{E_R^2 + E_I^2} \end{aligned} \tag{9}$$

$\mathbf{J}^\Gamma$ and $\mathbf{J}^\Phi$ are Jacobian submatrices. $\Delta\Gamma(E(\omega))$, where $\Delta\Gamma(E(\omega)) = \ln(E^{\text{meas}}(\omega)) - \ln\left(E^{\text{calc}}(\omega)\right)$ are the differences in log-amplitude between measured and calculated field values at the receivers, and $\Delta\Phi(E(\omega))$, where $\Delta\Phi(E(\omega)) = \arg(E^{\text{meas}}(\omega)) - \arg\left(E^{\text{calc}}(\omega)\right)$, are the differences in unwrapped phases [40]. In practice, the Gauss-Newton algorithms described in equations (7) and (8) are ill-posed and can only be successfully used by applying appropriate regularization techniques [42]–[44].

B. Dispersion Model

The electrical property dispersion relationships can vary significantly from one material to another. Accurate characterization over a large frequency spectrum such as 10 MHz–100 GHz is quite difficult due to multiple relaxations mechanisms [4]. Fortunately, within a narrower microwave frequency band used in medical microwave imaging, most biological tissue and coupling media investigated to date [2], [54] follow a smooth characteristic function enabling us to utilize simple functional representations. The linear model is the most straightforward case where an individual electrical property can be represented in a two term expression as

$$V = A\,W + B \tag{10}$$

where V can be either ε_r (or σ) or $\ln(\varepsilon_r)$ (or $\ln(\sigma)$) and W represents either ω or $\ln(\omega)$ and A and B are linear coefficients. The use of the logarithm function allows us to assume linear-linear, log-linear, linear-log or log-log relationships, respectively. For example, $\varepsilon_r = A\,\ln(\omega) + B$ is referred as the log-linear model. For sufficiently narrow frequency intervals, the linear-linear model quite often is a good approximation. The traditional single frequency reconstruction can be regarded as a limiting case of the MFDR algorithm where A is simply set to zero.

Important factors to consider when choosing an appropriate frequency dispersion model for the image reconstruction algorithm include:

1) the dispersion model will be applied identically to all materials in the imaging zone. For this type of imaging, *a priori* knowledge concerning the dispersion characteristics of the target and medium may be useful, and
2) the MFDR algorithm is general enough to accommodate more complicated dispersion models than those suggested above. Such a model could be utilized for a variety of complex relationships over a large frequency range; however, the consequences would include reconstructing more unknowns which could increase the possibility of convergence instability.

C. Row and Column Weighting

We have previously described a pre-scaling approach to balance the influence of the permittivity parameters to their associated conductivity values [48]. Generally, the image reconstruction process produces higher quality images when the magnitudes of these parameters are roughly balanced. This scaling approach falls under the general heading of matrix row and column weighting [45], [55] in solving least-square problems. As we progress to reconstructing the dispersion coefficients themselves instead of the actual properties, the parameter scaling clearly becomes more complex. In general, the weighted system of equations can be written in the form (where the equation $Ax = b$ is formed from either equations (7) or (8). In this case, A is the Jacobian matrix and x is the same unknown vector as in (7) and (8))

$$(D_R A D_C)\left(D_C^{-1}x\right) = (D_R b) \tag{11}$$

where D_R and D_C are the row and column diagonal weighting matrices, and A, x and b are the conventional left-hand-side (LHS) matrix, unknown and right-hand-side (RHS) vectors, respectively. For the problems described in equations (7) and (8), the dimensions of A, x and b are $(2TR \times F) \times (P \times M + P \times N)$, $P \times (M + N)$, and $(2TR \times F)$, respectively. In equation (11), the problem is initially solved for least square solution of $\left(D_C^{-1}x\right)$ instead of simply x from which x can then eventually be extracted through multiplication by D_C

$$x = D_C\left(D_C^{-1}x\right)_{LS} \tag{12}$$

Diagonal matrix D_R can be used to form a weighted least-square problem through which we can adjust the weights of the measurement data at different frequencies or weights between log-magnitude and phase.

D. Time-Domain Forward Computation

As was demonstrated in Fang *et al* [53], the most significant computational time expense for a Gauss-Newton iterative approach (utilizing the adjoint technique) is the calculation of the forward electric field solutions at each iteration (in fact, it was shown that the construction of the Jacobian matrix terms – previously identified as the largest time expense – could be reduced to simple inner products of the various forward electric field solution pairs associated with different illuminating antennas and a pre-computed weighting vector – i.e. the adjoint technique). Utilizing the previously developed frequency domain technique [40], [56], implementation of the MFDR approach would increase the computation time linearly based on the number of frequencies used. However, implementation of a time-domain electric field forward solution can offer significant benefits because the required multiple frequency solutions can be extracted from a single time-domain solution. In practice, a finite-difference time-domain (FDTD) [57] approach utilizing a differential Gaussian pulse could be used to generate the time domain response. The pulses would be applied individually at each transmitting antenna followed by a fast Fourier transform (FFT) of the signal responses at each receiver to recover the associated single frequency response. While the computation time for performing the Fourier transformations is not significant, it still constitutes a considerable time savings compared to solving multiple frequency domain forward solutions at each frequency (i.e. computing numerous matrix back substitutions). For a typical reconstruction problem size, a factor of roughly 2 in computation time reduction is achieved by using the time-domain/FFT approach when 5 frequencies are applied.

III. Results

In this section, we present three examples to illustrate image reconstruction improvements utilizing this technique. These examples focus on 2-D reconstructions utilizing transverse-magnetic (TM) microwave illuminations. Sixteen monopole antennas are positioned equally about the perimeter of a 15 cm diameter circle [10]. The data sets consist of electric field measurements at all 15 receivers for a given transmitting antenna with the target region being illuminated sequentially by each of the 16 antennas individually (Note that for the actual measured data, the electronics channels associated with each antenna can operate in both transmit and receive modes).

For all forward calculations including the generation of simulated measurement in example 1, a 2-D FDTD solver is used with generalized perfectly matched layer (GPML) [58] truncating the mesh. The grid size for the forward domain is 110×110 for a total size of 18.8 cm×18.8 cm surrounded by 12 layers of GPML. For each excitation, a monochromatic wave is applied at the location of each antenna. The amplitudes and phases of steady state fields are then extracted by a fast two-point algorithm [59]. A dual-mesh [60] scheme is also used for these reconstructions. The circular parameter mesh consists of 281 nodes with 524 associated linear triangular elements concentrically placed within antenna array. A diagram of the forward mesh, reconstruction parameter mesh and antenna array is shown in Fig. 1.

The reconstruction algorithm utilizes a hybrid of a Tikhonov regularization and Levenberg-Marquardt(L-M) process as described in Meaney *et al* [16] with the L-M regularization weight fixed at 0.1 and that of the Tikhonov algorithm set at 0.5. A spatial filter technique [44] is applied in both examples with the averaging factor set to 0.1 for the simulation and 0.4 for phantom reconstructions, respectively. The algorithm was allowed to process 30 iterations in example 1 and 20 iterations for example 2. Recognizing that the output of the MFDR algorithm is a spectrum of dispersion coefficient distributions

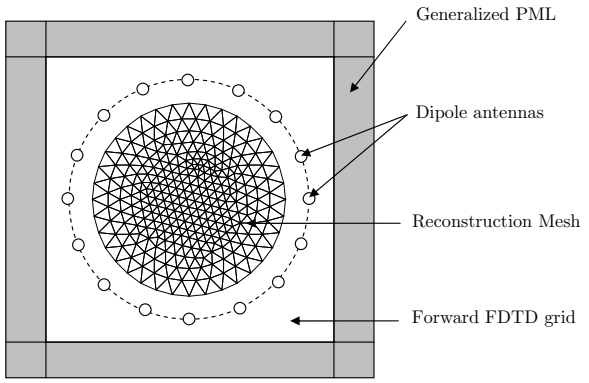

Fig. 1. Schematic diagram of the simulated illumination tank describing the spatial relationship between the forward field calculation problem (FDTD grid, antenna locations and GPML) to the reconstruction problem (parameter reconstruction mesh).

which by themselves do not actually have physical meaning, we have interpolated all results to the dielectric profiles at 900 MHz based on the selected dispersion model for all cases, unless otherwise noted, to simplify the comparisons.

The first example is a simulation of a large/high-contrast, two-region object consisting of frequency varying materials to mimic a breast with a large inclusion. This example is intended to demonstrate the performance of MFDR under ideal conditions. In addition to the first example, we present a second simulation which exploits the notion of visualizing the dispersion coefficients directly to enhance the low-contrast object recovery. In the third example, we reconstruct images of a cylindrical molasses phantom with a saline inclusion from actual measured data. The measurement data is acquired using the prototype system described in [10] with a background medium comprised of a 50:50 glycerin:water mixture [54]. The relative permittivities and conductivities of the background, object and inclusion were measured using an HP85070B dielectric probe kit in conjunction with an HP8753C Network Analyzer.

A log-log dispersion model was chosen in the first simulation case, while, a linear-linear model is assumed in the reconstruction of the molasses phantom from actual measurement data. All reconstructions were initialized as a homogeneous domain with the actual background dispersion coefficients. Before starting the process, a least squared regression process was used to establish the dispersion coefficients of the background permittivity and conductivity from actual probe measurements. All computations were performed on a Compaq AlphaServer 833 MHz ES40 workstation. The computation time for each iteration included roughly 2 seconds per frequency to calculate the forward field solutions for 16 transmitting antennas using 4 CPU's in parallel and roughly 1 second to solve for the dispersion coefficient update vector on a single CPU.

A. Simulation Experiments

A 10.2 cm diameter cylindrical object with a 3.0 cm diameter inclusion located in the lower left quadrant is used in the simulation. Properties equivalent to that of 0.9% saline are used as the background coupling medium to generate a high contrast imaging problem that would normally be difficult to reconstruct in a single frequency scheme. The properties for the object and inclusion roughly mimic that for breast fat and glandular tissue respectively [2]. The property dispersion curves for the background, object and inclusion used in this simulation are plotted in Fig. 2.

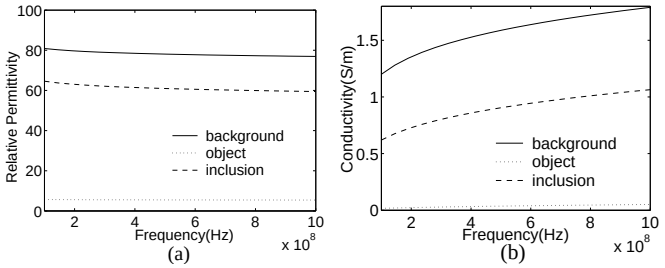

Fig. 2. Simulated dispersion curves for the materials used in the simulation (a) relative permittivity, (b) conductivity.

Fig. 3 shows the recovered relative permittivity and conductivity images for several single and multiple frequency reconstructions utilizing the log-log dispersion model. While the 300 MHz case converges to a stable image, the properties are quite smoothed over the domain (the inclusion appears only as an indentation in the object perimeter) as would be expected because of the reduced resolution associated with the lower frequencies. For both higher, single frequency cases (600 and 900 MHz), the images have clearly converged to non-interesting solutions suggesting that the measurement data in these two cases individually do not contain sufficient information to recover stable images. The two frequency case utilizing 300 and 600 MHz recovers an accurate representation of the phantom with the inclusion more accurately defined than for the 300 MHz case alone while a similar two frequency case using 600 and 900 MHz cannot recover a useful image. It is clear that the algorithm benefits from both the stabilizing effects of the lower frequency data along with the higher resolution capabilities of the higher frequency reconstruction. The images for the three (300, 600 and 900 MHz) and four (300, 500, 700 and 900 MHz) frequency cases converge to similar solutions to that of the combined 300 and 600 MHz case suggesting again that the 300 MHz data is vital for convergence stability but that the increased higher frequency data has diminished impact.

Fig. 4 illustrates the RMS error (e_{RMS}) between the true and recovered electrical property values as a function of iteration number for the seven cases discussed above. e_{RMS} is defined as

$$e_{RMS} = \sqrt{\frac{\sum_{i=1}^{P} \left(V_i^{\text{true}} - V_i^{\text{recon}}\right)^2}{P}} \tag{13}$$

where V stands for either ε_r or σ and P is the number of reconstruction parameters. These are also plotted for the dispersion relationship defined 900 MHz values. Similar to the qualitative results in Fig. 3, e_{RMS} does not decrease significantly for either the ε_r or σ cases with iteration for

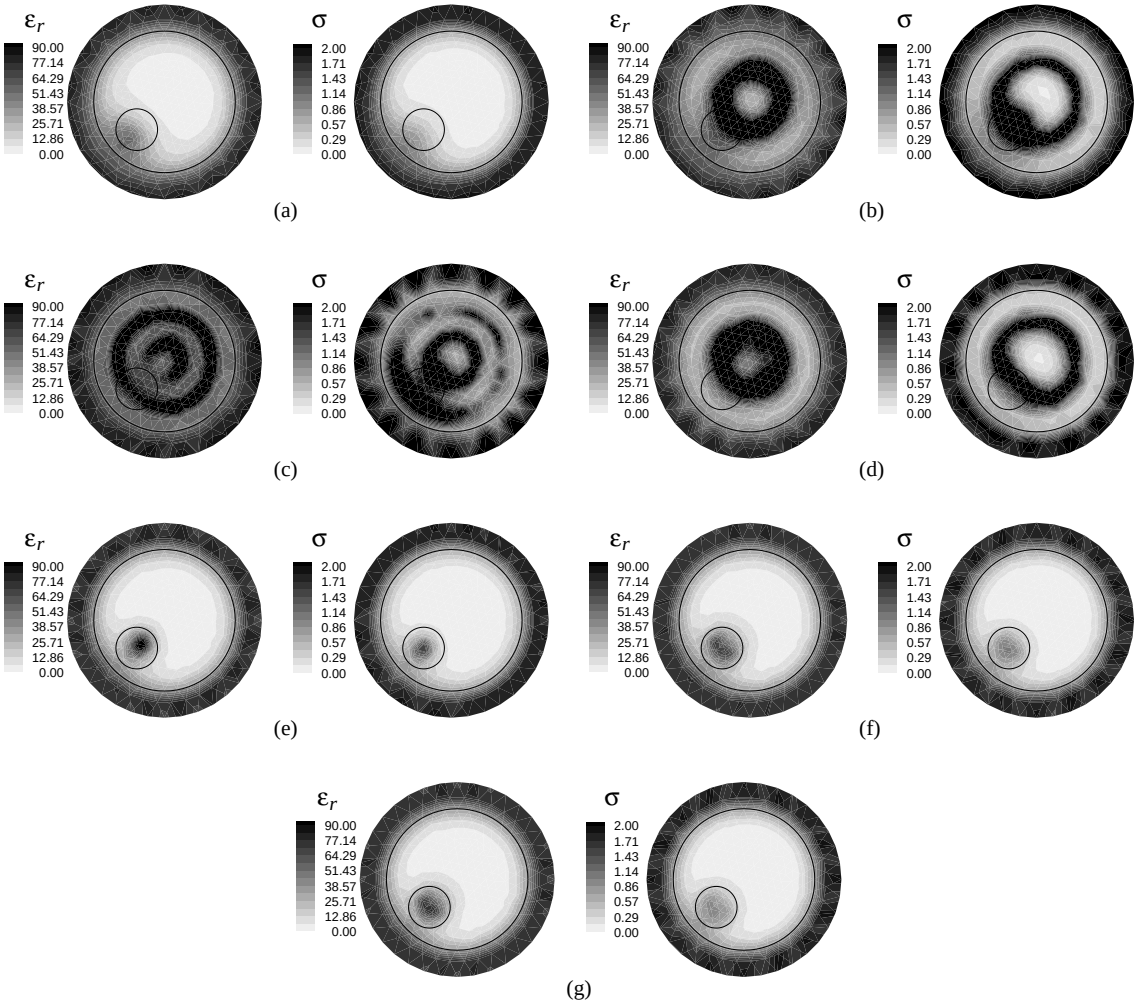

Fig. 3. Reconstructed permittivity and conductivity images of a 10.2 cm diameter breast-like object with a 3.0 cm diameter tumor-like inclusion at (a) 300 MHz, (b) 600 MHz, (c) 900 MHz, (d) 600/900 MHz, (e) 300/600 MHz, (f) 300/600/900 MHz, (g) 300/500/700/900 MHz using simulated data.

either the 600, 900 or 600/900 MHz cases which would be expected since all of the images in these cases converge to non-interesting solutions. Of the remaining of the cases, the 300 MHz error plots converge to the highest values for both ε_r and σ which would also be expected since these are the least spatially resolved. The remaining three converge to nearly the same σ error value; however, the three and four frequency reconstructions converge to a slightly improved ε_r error compared with the 300/600 MHz case. This suggests that the addition of more frequency data does improve the images somewhat but that increasing the amount of data beyond the three frequency sets in this situation has minimal impact.

The previous example shows the advantages of MFDR in a high contrast image reconstruction situation; however, the approach also works well in lower contrast cases. In this particular low contrast case, the object is difficult to distinguish from dielectric images at individual frequencies while its dispersion characteristics might provide significant contrast from that of the background which can be exploited by MFDR. For this example, we removed the 10.2cm diameter object from the previous case and retain the inclusion. The inclusion and background media were characterized by a linear-log dispersion model: permittivity (a) background, $A_{\varepsilon_r} = -6.98 \times 10^{-11}, B_{\varepsilon_r} = 3.70$, (b) inclusion, $A_{\varepsilon_r} = 9.67E \times 10^{-11}, B_{\varepsilon_r} = 2.85$. For the conductivity component, the inclusion and background are identical having $A_\sigma = 8.41 \times 10^{-11}, B_\sigma = -0.662$. The permittivity dispersion curves of the inclusion and background are plotted in Fig. 5 (a). Using the LMPF-MFDR reconstruction with simulated measurement data at 600/900 MHz, $A_{\varepsilon_r}, B_{\varepsilon_r}$ and conductivity dispersion coefficients were successfully reconstructed. The recovered A_{ε_r} image (Fig. 5 (b)) clearly shows the distinct dispersion characteristics of the inclusion. Based on the dispersion model, equation (10), the permittivity distributions were also computed at 600 MHz and 900 MHz and shown in Fig. 5 (c) and (d). The inverted contrast of the object relative to the background can be observed as the result of the dispersion reconstruction.

B. Phantom Experiments

Fig. 7 shows the reconstructed images utilizing a linear-linear dispersion model of a 10.1 cm diameter cylinder of

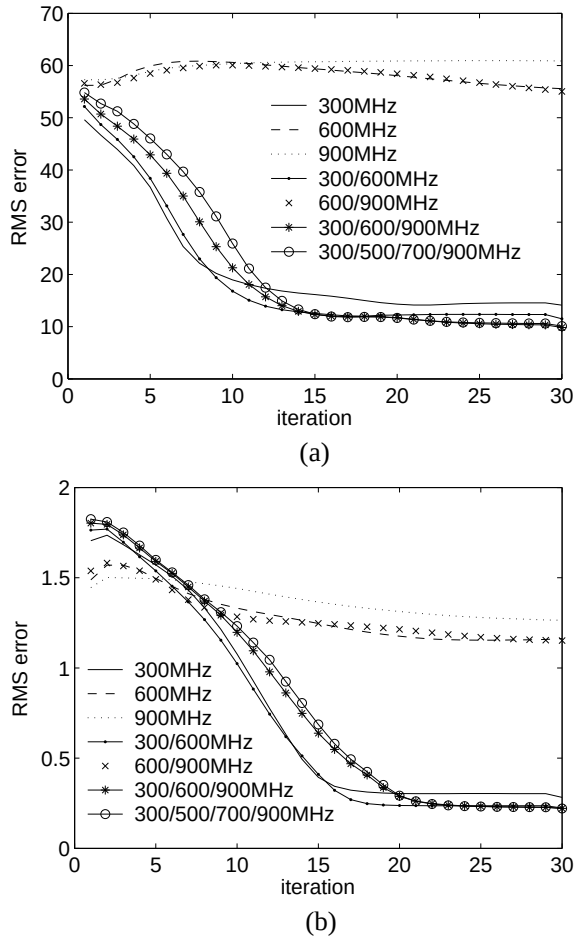

Fig. 4. Plots of the (a) ε_r and (b) σ RMS errors between the actual and recovered properties as a function of iteration for all seven imaging cases shown in Fig. 3.

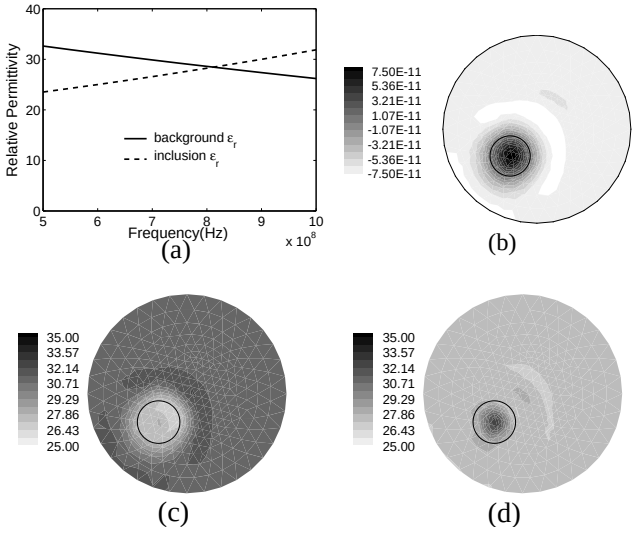

Fig. 5. Utilization of dispersion coefficients: (a) relative permittivity dispersion curves, (b) reconstructed A_{ε_r}, (c) computed ε_r at 600 MHz and (d) 900 MHz.

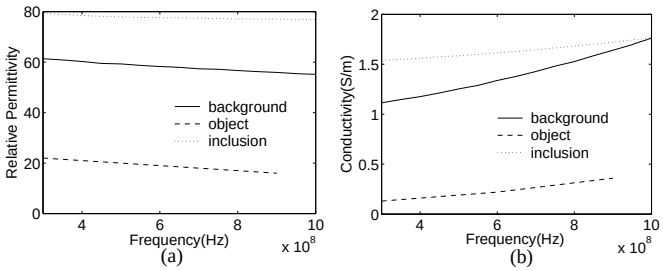

Fig. 6. Measured electrical properties for the materials used in the phantom experiment: (a) relative permittivity, (b) conductivity.

molasses with a 3.1 cm diameter 0.9% saline inclusion offset upwards within the molasses. The entire molasses cylinder is also positioned 0.6 cm upwards from the center of the array and is surrounded by a background medium comprised of 50% Glycerin and 50% water. The electrical properties of the three liquids are plotted versus frequency in Fig. 6.

Similar to the first simulation case, the ε_r image for the 500 MHz case shows the rough outline of the cylinder with an indentation near its top surface corresponding to the saline inclusion. The recovered object in the associated conductivity image is smaller in size than its permittivity counterpart (typical for our lower frequency images [61]) with no apparent indication of any inclusion. The property values are nominally correct and the least squared electric field error (LSE) plot does not suggest that this solution has diverged (not shown). Similar to the simulation cases in Section III.A, the higher frequency case (900 MHz) has converged to a non-interesting image. The two multi-frequency cases have converged to significantly better resolved images compared with the 500 MHz case. In both cases the outline of the molasses phantom is clearly defined in both permittivity and conductivity images with the location of the inclusion consistently more accurately recovered in the permittivity component. Additionally, the property distribution of the molasses appears to be more uniform and the recovered values of the inclusion are more accurate for the three frequency case. Similar quality images were achieved utilizing the log-log dispersion model and are not shown.

IV. Discussion and Conclusions

We have developed a dispersion characteristic reconstruction technique which facilitates the synergy of multiple frequency measurements into a single image reconstruction process. Utilization of lower frequency data alone can often produce low resolution images in a stable manner while reconstructions using higher frequency data alone (especially when imaging large, high contrast objects such as the breast) often result in non-meaningful results. For the algorithms presented here, we simultaneously utilize measurement data over a broad frequency range and recover frequency independent coefficients associated with assumed underlying property dispersion relationships. While images at discrete frequencies can be extracted by applying the dispersion relationships after the reconstruction is processed, the dispersion coefficients themselves may provide additional diagnostic information.

We specifically chose imaging problems for large, high-contrast objects to demonstrate the capabilities of this approach; that is the single frequency algorithm was known to

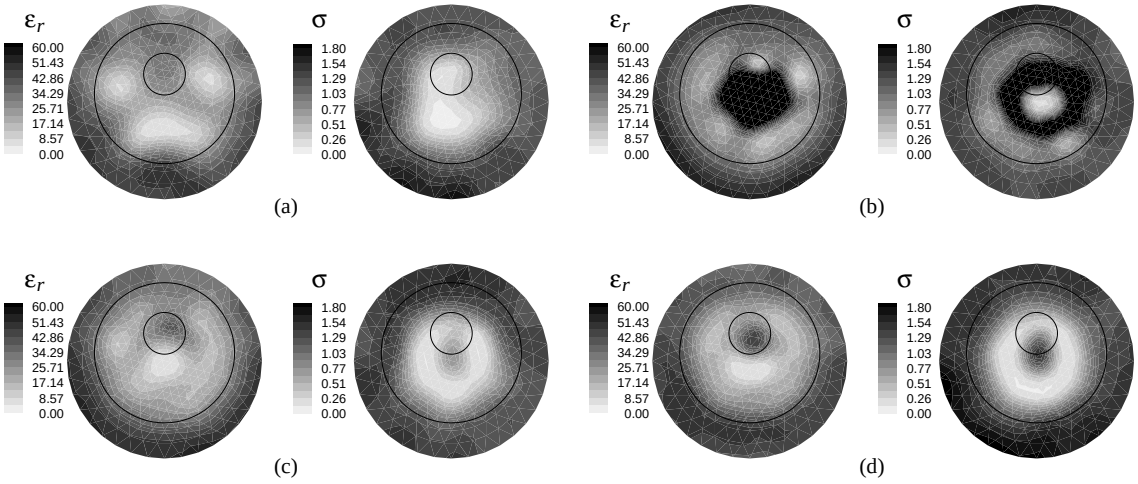

Fig. 7. Reconstructed permittivity and conductivity images of a 10.1 cm diameter cylinder of molasses with a 3.1 cm diameter saline inclusion at (a) 500 MHz, (b) 900 MHz, (c) 500/900 MHz, (d) 300/500/900 MHz using measurement data.

diverge for the higher frequency cases without the assistance of *a priori* information. In both simulations and phantom experiments, it is clear that we can only utilize the higher frequency data when combined with that for a lower frequency. In addition, as the amount of higher frequency data is increased, there is a slight improvement in the image quality. While we would naturally expect resolution improvement whenever any new data is added, the level of independence of the new data from the existing data may be compromised when the selected frequencies are closely packed. This will be an important point of further investigation as we work towards utilizing the higher frequency (up to 2.5 GHz) data available with our new data acquisition system [62].

Additionally, there remain several techniques by which the performance of this approach can be fine-tuned. As we work towards the development of a lower contrast coupling medium for our breast imaging system, the single frequency algorithm can often recover a stable image, even at higher frequencies because of the lower contrast. It will be important to study the effects of the dispersion model choice, along with the amount and span of the additional frequency information in conjunction with existing reconstruction enhancement capabilities such as row and column weighting and our 2-step regularization approach [44] to optimize the system resolution.

REFERENCES

[1] L. E. Larsen, and J. H. Jacobi, *Medical applications of microwave imaging*, New York: IEEE, 1986.

[2] S. Gabriel, R. W. Lau, and C. Gabriel, "The dielectric properties of biological tissues: II. Measurements in the frequency range 10 Hz to 20 GHz," *Physics in Medicine and Biology*, vol. 41, pp. 2251-2269, 1996.

[3] W. T. Joines, Y. Zhang, C. Li, and R. L. Jirtle, "The measured electrical properties of normal and malignant human tissues from 50 to 900 MHz," *Med. Phys.*, vol. 21, pp. 547-550 1994.

[4] K. R. Foster, and J. L. Schepps, "Dielectric properties of tumor and normal tissues at radio through micro-wave frequencies," *Journal of Microwave Power*, vol. 16, pp. 107-119, 1981.

[5] H. Q. Woodward, and D. R. White, "The composition of body tissues," *The British Journal of Radiology*, vol. 59, pp. 1209-1219, 1986.

[6] S. Y. Semenov, A. E. Bulyshev, A. E. Souvorov, R. H. Svenson, Y. E. Sizov, V. Y. Borisov, V. G. Posukh, I. M. Kozlov, A. G. Nazarov, and G. P. Tatsis, "Microwave tomography: Theoretical and experimental investigation of the iteration reconstruction algorithm," *IEEE Trans. Microwave Theory Tech.*, vol. 46, pp. 133- 141, 1998.

[7] S. Y. Semenov, R. H. Svenson, A. E. Bulyshev, A. E. Souvorov, A. G. Nazarov, Y. E. Sizov, V. G. Posukh, and A. Pavlovsky, "Three-dimensional microwave tomography: Initial experimental imaging of animals," *IEEE Trans. Biomed. Eng.*, vol. 49, pp. 55-63, 2002.

[8] S. S. Chaudhary, R. K. Mishra, A. Swarup, and J. M. Thomas, "Dielectric properties of normal and malignant human breast tissues at radiowave and microwave frequencies," *Indian J. Biochem. Biophys*., vol. 21, pp. 76-79, 1984.

[9] D. Colton, and P. Monk, "A new approach to detecting leukemia: using computational electromagnetics," *IEEE Trans. on Comp. Sci. and Eng.*, vol. 2, pp. 46-52, 1995.

[10] P. M. Meaney, M. W. Fanning, D. Li, S. P. Poplack, and K. D. Paulsen, "A clinical prototype for active microwave imaging of the breast, " *IEEE Trans. Microwave Theory Tech.*, vol. 48, pp. 1841-1853, 2000.

[11] S. C. Hagness, A. Taflove, and J. E. Bridges, "Two-dimensional FDTD analysis of a pulsed microwave confocal system for breast cancer detection: Fixed-focus and antenna-array sensors," *IEEE Trans. Biomedical Engineering*, vol. 45, pp. 1470-1479, Dec. 1998.

[12] E. J. Bond, X. Li, S. C. Hagness, and B. D. van Veen, "Microwave imaging via space-time beamforming for early detection of breast cancer," *IEEE Trans. on Antennas Propagat.*, vol. 51, pp. 1690-1705, 2003.

[13] E. C. Fear, X. Li, S. C. Hagness, and M. A. Stuchly, "Confocal microwave imaging for breast cancer detection: localization of tumors in three dimensions," *IEEE Trans. Biomed. Eng.*, vol. 49, pp. 812-822, 2002.

[14] E. C. Fear, J. Sill, and M. A. Stuchly, "Experimental feasibility study of confocal microwave imaging for breast tumor detection," *IEEE Trans. Microwave Theory Tech.*, vol. 51, pp. 887-892, 2003.

[15] R. Pethig, "Dielectric properties of biological materials: biophysical and medical applications," *IEEE Trans. on Elec. Insulation*, vol. 19, pp. 453-474, 1984.

[16] P. M. Meaney, M. W. Fanning, K. D. Paulsen, D. Li, S. A. Pendergrass, Q. Fang, and K. L. Moodie, "Microwave thermal imaging: Initial *in vivo* experience with a single heating zone," *Int. J. of Hyperthermia*, 2003 (in press).

[17] L. E. Larsen, and J. H. Jacobi, "Methods of active microwave imagery for dosimetric applications," in *Medical Applications of Microwave Imaging*, New York: IEEE Press, pp.118-137, 1986.

[18] J. C. Bolomey, J. Izadnegahdar, L. Jofre, C. H. Pichot, G. Peronnet, and M. Solaimani, "Microwave diffraction tomography for biomedical applications," *IEEE Trans. Microwave Theory Tech.*, vol. 30, pp. 1990-2000, 1982.

[19] R. Maini, M. F. Iskander, and C. H. Durney, "On electromagnetic

imaging using linear reconstruction techniques," *Proceedings of the IEEE*, vol. 68, pp. 1550-1552, 1980.
[20] A. J. Devaney, "A computer simulation study of diffraction tomography," *IEEE Transaction on Biomedical Engineering*, vol. 30, pp. 377-386, 1983.
[21] C. M. Sehgal, G. M. Brown, R. C. Bahn, and J. F. Greenleaf, "Measurement and use of acoustic nonlinearity and sound speed to estimate composition of excised livers," *Ultrasound in Medicine and Biology*, vol. 12, pp. 865-874, 1986.
[22] C. R. Hill, *Physical principles of medical ultrasonics*, Ellis Horwood Limited, Chichester, England, 1986.
[23] M. Slaney, A. C. Kak, and L. E. Larsen, "Limitations of imaging with first-order diffraction tomography," *IEEE Trans. Microwave Theory Tech.*, vol. 32, pp. 860-874, 1984.
[24] M. Miyakawa, K. Orikasa, M. Bertero, P. Boccacci, F. Conte, and M. Piana, "Experimental validation of a linear model for data reduction in chirp-pulse microwave CT," *IEEE Trans. Med. Imag.*, vol. 21, pp. 385-395, 2002.
[25] S. Jacobsen, and P. R. Stauffer, "Multifrequency radiometric determination of temperature profiles in a lossy homogeneous phantom using a dual-mode antenna with integral water bolus," *IEEE Trans. Microwave Theory Tech.*, vol. 50, pp. 1737-1746, 2002.
[26] S. D. Prionas, and G. M. Hahn, "Noninvasive thermometry using multiple-frequency-band radiometry: a feasibility study," *Bioelectromagnetics*, vol. 6, pp. 391-404, 1985.
[27] S. Jacobsen, and P. R. Stauffer, "Non-parametric 1-D temperature restoration in lossy media using Tikhonov regularization on sparse radiometry data," *IEEE Trans. Biomed. Eng.*, vol. 50, pp. 178-188, 2002.
[28] K. Maruyma, S. Mizushina, T. Sugiura, G. M. J. van Leeuwen , J. W. Hand, G. Marrocco, F. Bardati, A. D. Edwards, D. Azzopardi, and D. Land, "Feasibility of noninvasive measurement of deep brain temperature in newborn infants by multifrequency microwave radiometry," *IEEE Trans. Microwave Theory Tech.*, vol. 48, pp. 2141-2147, 2000.
[29] S. Mouty, B. Bocquet, R. Ringot, N. Rocourt, and P. Devos, "Microwave radiometric imaging for the characterisation of breast tumors," *European Physical Journal: Applied Physics*, vol. 10, pp. 73-78, 2000
[30] K. L. Carr, "Microwave radiometry: its importance in the detection of cancer," *IEEE Trans. Microwave Theory Tech.*, vol. 37, pp. 1862-1869, 1989.
[31] K. L. Carr, P. Cevasco, P. Dunlea, and J. Shaeffer, "Radiometric sensing: an adjuvant to mammography to determine breast biopsy," *IEEE MTT-S International Microwave Symposium Digest*, vol. 2, pp. 929-932, 2000.
[32] J. T. Ylitalo, and H. Ermert, "Ultrasound synthetic aperture imaging: monostatic approach," *IEEE Trans. on Ultrasonics, Ferroelectrics and Frequency Control*, vol. 41, pp. 333-339, 1994.
[33] C. H. Frazier, and W. D. O'Brien, Jr., "Synthetic aperture techniques with a virtual source element," *IEEE Trans. on Ultrasonics, Ferroelectrics and Frequency Control*, vol. 45, pp. 196-207, 1998.
[34] X. Li, S. C. Hagness, B. D. van Veen, and D. van der Weide, "Experimental investigation of microwave imaging via space-time beamforming for breast cancer detection," *2003 IEEE MTT-S International Microwave Symposium Digest*, vol. 1, pp. 379-382, 2003.
[35] R. A. Kruger, W. L. Kiser Jr., D. R. Reinecke, G. A. Kruger, and R. L. Eisenhart, "Thermoacoustic computed tomography of the breast at 434 MHz", *IEEE MTT-S International Microwave Symposium Digest*, pp. 591-594, 1999.
[36] L. V. Wang, X. Zho, H. Sun, and G. Ku, "Microwave-induced acoustic imaging of biological tissues," *Rev. Sci. Instrum.*, vol. 70, pp. 3744-3748, 1999.
[37] S. Caorsi, G. L. Gragnani, and M. Pastorino, "Reconstruction of dielectric permittivity distributions in arbitrary 2D inhomogeneous biological bodies by a multiview microwave numerical method," *IEEE Trans. Med. Imag.*, vol. 12, pp. 232-239, 1993.
[38] N. Joachimowicz, C. Pichot, and J. P. Hugonin, "Inverse scattering: an iterative numerical method for electromagnetic imaging," *IEEE Trans. on Antennas Propagat.*, vol. 39, pp. 1742-1752, 1991
[39] Q. H. Liu, Z. Q. Zhang, T. T. Wang, J. A. Bryan, G. A. Ybarra, L. W. Nolte, and W. T. Joines, "Active microwave imaging. I. 2-D forward and inverse scattering methods," *IEEE Trans. Microwave Theory Tech.*, vol. 50, pp. 123-133, 2002.
[40] P. M. Meaney, K. D. Paulsen, B. W. Pogue, and M. I. Miga, "Microwave image reconstruction utilizing log-magnitude and unwrapped phase to improve high-contrast object recovery," *IEEE Trans. Med. Imag.*, vol. 20, pp. 104-116, 2001.
[41] B. Kaltenbacher, "Newton-type methods for ill-posed problems," *Inverse Problems*, vol. 13, pp. 729-753, 1997.
[42] A. N. Tikhonov, and V. Y. Arsenin, *Solutions of ill-posed problems*, John Wiley & Sons, New York, 1977.
[43] S. Caorsi, S. Ciaramella, G. L. Gragnani, and M. Pastorino, "On the use of regularization techniques in numerical inverse scattering solutions for microwave imaging applications," *IEEE Trans. Microwave Theory Tech.*, vol. 43, pp. 632-640, 1995.
[44] P. M. Meaney, E. Demidenko, N. K. Yagnamurthy, D. Li, M. W. Fanning, and K. D. Paulsen, "A two-stage microwave image reconstruction procedure for improved internal feature extraction," *Med. Phys.*, vol. 28, pp. 2358-2369, 2001.
[45] G. H. Golub, and C. H. van Loan, *Matrix Computations*, The Johns Hopkins University Press, Baltimore, MD, 1991.
[46] W. C. Chew, and J. H. Lin, "A frequency-hopping approach for microwave imaging of large inhomogeneous bodies,", *IEEE Microwave and Guided Wave Letters*, vol. 5, pp. 439-441, 1995
[47] O. S. Haddadin, and E. S. Ebbini, "Imaging strongly scattering media using a multiple frequency distorted Born iterative method," *IEEE Trans. on Ultrasonics, Ferroelectrics and Frequency Control*, vol. 45, pp. 1485-1496, 1998
[48] P. M. Meaney, N. K. Yagnamurthy, and K. D. Paulsen, "Pre-scaling of reconstruction parameter components to reduce imbalance in image recovery process," *Physics in Medicine and Biology*, vol. 47, pp. 1101-1119, 2002
[49] A. Ishimaru, *Electromagnetic wave propagation, radiation and scattering*, Chapter 8, Prentice Hall, New Jersey, 1991
[50] K. S. Cole, and R. H. Cole, "Dispersion and absorption in dielectrics: I. Alternating current characteristics," *J. of Chem. Phys.*, pp. 341-351, 1941
[51] S. Gabriel, R. W. Lau, and C. Gabrial, "The dielectric properties of biological tissues: III. Parametric models for the dielectric spectrum of tissues," *Phys. in Medicine and Biology*, vol. 41, pp. 2271-2293, 1996.
[52] F. A. Duck, *Physical properties of tissue: a comprehensive reference book*, London, Academic Press, 1990.
[53] Q. Fang, P. M. Meaney, S. D. Geimer, A. V. Streltsov, and K. D. Paulsen, "Microwave image reconstruction from 3D fields coupled to 2D parameter estimation," *IEEE Trans. Med. Imag.*, vol. 23, pp. 475-484, Apr. 2004.
[54] P. M. Meaney, S. A. Pendergrass, M. W. Fanning, D. Li, and K. D. Paulsen, "Importance of using a reduced contrast coupling medium in 2D microwave breast imaging," *Journal of Electromagnetic Waves and Applications*, vol. 17, pp. 333-355, 2003.
[55] C. L. Lawson, and R. J. Hanson, *Solving Least Squares Problems*, Englewood Cliffs, NJ: PrenticeHall, pp. 183-188, 1974.
[56] P. M. Meaney, K. D. Paulsen, and T. P. Ryan, "Two-dimensional hybrid element image reconstruction for TM illumination," *IEEE Trans. Antennas Propagat.*, vol. 43, pp. 239-247, 1995.
[57] A. Taflove, and S. C. Hagness, *Computational electrodynamics: the finite-difference time-domain method*, Artech House, Boston, MA, 2000.
[58] J. Fang, and Z. Wu, "Generalized perfectly matched layer for the absorption of propagating and evanescent waves in lossless and lossy media," *IEEE Trans. Microwave Theory Tech.*, vol. 44, pp. 2216-2222, 1996.
[59] U. Oğuz, and L. Gürel, "Interpolation techniques to improve the accuracy of the plane wave excitations in the finite-difference time-domain method," *Radio Sci.*, vol. 32, pp. 2189-2199, 1997.
[60] K. D. Paulsen, P. M. Meaney, M. J. Moskowitz, and J. M. Sullivan Jr., "A dual mesh scheme for finite element based reconstruction algorithms," *IEEE Trans. Med. Imag.*, vol. 14, pp. 504-514, 1995.
[61] P. M. Meaney, K. D. Paulsen, and J. T. Chang "Near-field microwave imaging of biologically based materials using a monopole transceiver system," *IEEE Trans. Microwave Theory Tech.*, vol. 46, pp.31-45, 1998.
[62] D. Li, P. M. Meaney, T. Raynolds, S. A. Pendergrass, M. W. Fanning, and K. D. Paulsen, "A parallel-detection microwave spectroscopy for breast imaging," *IEEE Trans. on Instrumentation*, 2003 (submitted)

Qianqian Fang (S'03) was born in Anyang, Henan, China, in 1976. He received the B.Eng. degree in electrical engineering from the University of Electronic Science and Technology of China (UESTC), Chengdu, Sichuan, China, in 1999. He is currently working toward the Ph.D. degree in biomedical engineering at Thayer School of Engineering, Dartmouth College.

From 1997 to 1999, he was a Research Assistant with the microwave teaching and research group, UESTC, working with simulations and design of millimeter microwave circuits. In 1999, he jointed Computational Electromagnetics Lab, UESTC, implemented finite difference-time domain (FDTD) method with perfectly matched layer (PML) technique in EM pulse well-logging analysis. Since 2000, he has been a Research Assistant in microwave imaging group at Dartmouth College. His current research activities include three-dimensional image reconstruction algorithm, fast forward modeling using finite element method (FEM) and FDTD, regularization technique, phase unwrapping and theoretical analysis on non-linear tomographical imaging.

Mr. Fang is a student member of the IEEE Engineering in Medicine and Biology Society (IEEE-EMBS). He was the recipient of Herbert Darling Fellowship in 2000.

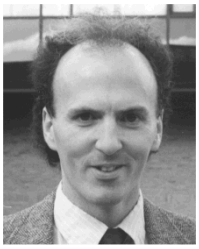

Paul M. Meaney (M'92) received A.B.'s in Computer Science and Electrical Engineering from Brown University in 1982, an M.S. in Electrical Engineering from the University of Massachusetts in 1985, and his Ph.D. in Biomedical Engineering from Dartmouth College in 1995.

He was a Postdoctoral Fellow at Dartmouth College from 1995-1996 and a NSF-NATO Postdoctoral Fellow at the Royal Marsden Hospital in Sutton, England from 1996-1997. He is currently a Research Associate Professor at Dartmouth College. His interests include developing microwave imaging for biomedical applications – especially breast imaging and hyperthermia monitoring, along with elastography and various applications of thermal modeling.

Keith D. Paulsen (S'85-M'86) received the B.S. degree in biomedical engineering from Duke University, Durham, NC, in 1981 and the M.S. and Ph.D. degrees in biomedical engineering from Dartmouth College, Hanover, NH, in 1984 and 1986, respectively.

From 1986 to 1988, he was an Assistant Professor in the Electromagnetics Group within the Department of Electrical and Computer Engineering, University of Arizona, Tucson. He is currently a Professor at the Thayer School of Engineering, Dartmouth College and the Director of the Radiobiology and Bioengineering Research Program for the Norris Cotton Cancer Center within the Dartmouth-Hitchcock Medical Center, Lebanon, NH. His research interests include computational methods with particular emphasis on biomedical problems in cancer therapy and imaging, and model-guided surgery.